Soft Matter

PAPER

View Article Online
View Journal | View Issue

Cite this: *Soft Matter*, 2025, 21, 7697

A unified approach to suspension cell mechanics

Muzaffar H. Panhwar, [abc] Peter Nestler,[ab] Yesaswini Komaragiri, [abc] Doreen Biedenweg,[ab] Bob Fregin, [abc] Eric Sündermann, [abc] Stefan Groß[cd] and Oliver Otto *[abc]

Received 23rd April 2025,
Accepted 25th August 2025

DOI: 10.1039/d5sm00414d

rsc.li/soft-matter-journal

Mechanical profiling of cells is crucial for diagnosis and monitoring of viral and chronic diseases. In particular, the Young's modulus of cells serves as a biological fingerprint that can be assessed, *e.g.*, by atomic force microscopy, micropipette aspiration, optical trapping and microfluidic methods. The diversity of these technologies with respect to timescale, strain rate and mechanical stress results in Young's moduli that cover orders of magnitude. Currently, it is unclear if these variations are of technical, physical or biological origin. Here, we exposed human leukaemia 60 (HL60) cells to mean hydrodynamic stress levels between 8 Pa and 800 Pa using real-time deformability cytometry. Our results follow a power law between applied stress and cellular Young's modulus and integrates seamlessly data from current state-of-the-art technologies into a unifying master curve. This renders suspension cell measurements independent from the experimental method, the timescale as well as the adhesion or suspension state. Finally, our data allows to calculate a resting Young's modulus, *i.e.*, in the absence of an external hydrodynamic stress that is independent of measurement buffer composition and viscosity. Considering the strong need for a standardized and quantifiable approach, we believe that our data present a step towards a universal application of cell mechanical phenotyping in life sciences.

Introduction

Mechanical profiling of cells is seen as a promising approach for diagnosis of bacterial and viral infections as well as to understand and monitor the onset of chronic diseases.[1–7] Numerous techniques such as atomic force microscopy (AFM),[8,9] optical stretching (OS),[10] optical trapping (OT),[11] deformability cytometry (DC),[12–17] shear flow deformability cytometry,[18] micropipette aspiration (MA),[19] magnetic tweezers (MT),[20] acoustically actuated bubbles,[21] and narrow-gap rheometry[22] have been established to assess cell mechanical properties. Of these properties the Young's modulus of cells is of particular interest since it is a measure of cell stiffness, which allows for label-free insights into regulatory processes associated with the cellular cytoskeleton. However, for a given cell line the reported Young's modulus values may vary by several orders of magnitude. For example, a cross-laboratory research on HL60 cells employed three methods to study cell mechanics: deformability cytometry,[12] microconstriction arrays,[14,23] and real-time deformability cytometry (RT-DC).[13] Significant differences in deformability have been reported, which could be attributed to a variation in the respective strain rates.[24] Another study, involving several technologies, indicated a Young's modulus of MCF-7 breast cancer cells that differs by three orders of magnitude, ranging from 4.5 Pa to 13.5 kPa.[25]

This apparent inconsistency renders a comparison between different studies nearly impossible. Often these variations are attributed to differences in experimental sensitivity, cell count, cell heterogeneity as well as measurement timescale and methods. Generally, experimental methods can be distinguished into those using a mechanical probe to indent cells locally (AFM, OT, MT)[8,9,11,20] and whole-cell deforming techniques (OS, DC).[10,12] Accordingly, variations in cell stiffness have been attributed to experimental aspects, *e.g.*, size and shape of the indenter, depth of indentation, and strain rate, as well as physiological effects, like the reorganization of the actin cortex and adaptation to the microenvironment.[24,25] However, even if the same technique is applied to investigate a particular cell line values vary considerably. For instance using AFM the Young's modulus of human embryonic kidney (HEK) cells is reported to be 6.5 kPa, 0.41 kPa or 0.26 kPa.[26] Therefore, it is essential to have access to an approach for reporting unified mechanical parameters of cells, independent of strain rates, timescales, and measurement conditions.

In order to better understand these variations in cell elasticity, we employed real-time deformability cytometry (RT-DC)

[a] *Zentrum für Innovationskompetenz: Humorale Immunreaktionen bei kardiovaskulären Erkrankungen, Universität Greifswald, Fleischmannstr. 42, Greifswald, 17489, Germany. E-mail: oliver.otto@uni-greifswald.de*
[b] *Institut für Physik, Universität Greifswald, Felix-Hausdorff-Strasse 6, 17489 Greifswald, Germany*
[c] *Deutsches Zentrum für Herz-Kreislauf-Forschung e.V., Standort Greifswald, Universitätsmedizin Greifswald, Fleischmannstr. 42, Greifswald, 17489, Germany*
[d] *Klinik für Innere Medizin B, Universitätsmedizin Greifswald, Fleischmannstr. 8, 17475 Greifswald, Germany*

and investigated HL60 cells under different environmental conditions. These include alterations in the sample buffer composition and buffer viscosity, cytoskeletal drug treatment as well as experimental assays at hydrodynamic stress levels varying over two orders of magnitude. Comparing measurements carried out in PBS buffer with RPMI as a native cell culture medium, our data on PBS yield for a given flow rate an increased cell size and a higher Young's modulus. This effect can be explained by the different shear stress amplitudes resulting from distinct buffer viscosities. We investigated the role of this stress-stiffening for suspension cell mechanics by varying the mean hydrodynamic stress between approximately 8 Pa and 800 Pa and compared our results to current state-of-art technologies like AFM, DC and OS. Our results yield a universal power-law between applied stress and cellular Young's modulus that is independent of measurement buffer, applied method and experimental timescale.

Results

In our study we used cell culture medium RPMI (complemented with 10% fetal calf serum (FCS) and 1% penicillin/streptomyosin (P/S)) and PBS complemented with 0.5% (w/v) methylcellulose (MC-PBS). Both buffers differ in composition but also in terms of viscosity and shear behaviour. For RPMI, bulk rheological measurements reveal a reduction in viscosity towards higher shear rates $\dot{\gamma}$, which plateaus for $\dot{\gamma} > 10\,383\ s^{-1}$ at a constant viscosity of η = 1.17 mPa s (see Materials and methods). On the contrary bulk MC-PBS is characterized by a shear-thinning behaviour over the full experimentally accessible range of shear rates (up to 40 000 s^{-1}). As a consequence, the viscosity of MC-PBS drops from approximately 14 mPa s (at 2000 s^{-1}) to 6 mPa s (at 40 000 s^{-1}, see Materials and methods and Fig. S1).

In the absence of hydrodynamic stress (reservoir condition), the mechanical analysis of HL60 cells reveals a deformation distribution with a mean value close to 0 independent of the measurement buffer (Fig. 1A and B, left panel). Cells display a circular shape as expected (Fig. 1A and B, left panel, insets). Upon exposure to normal and shear stress in a microfluidic channel, cells respond to the parabolic flow profile by a bullet-like shape (Fig. 1A and B, centre and right panel, insets). As flow rate is increased from 8 nL s^{-1} to 80 nL s^{-1}, deformation of RPMI suspended cells increases slightly from d = 0.009 ± 0.004 (mean ± standard deviation) to 0.014 ± 0.005 (Fig. 1A, centre and right panel), while MC-PBS suspended cells experience a substantial increase in deformation from d = 0.028 ± 0.009 to

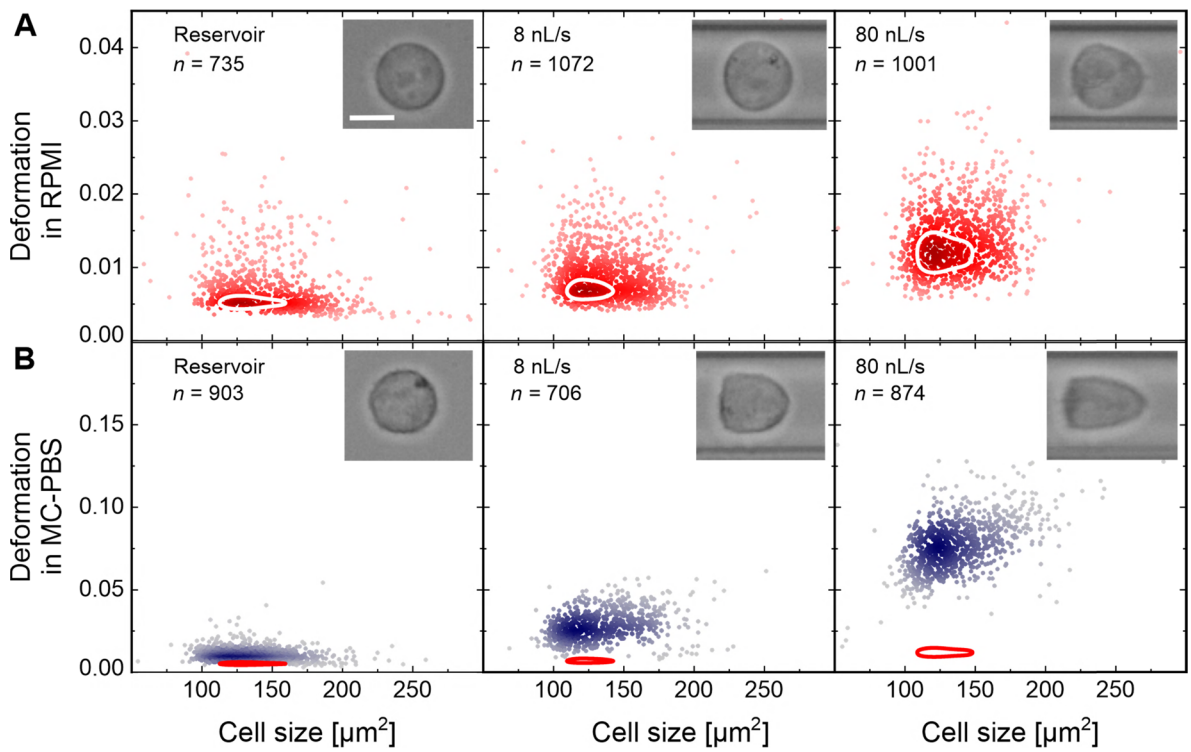

Fig. 1 Mechanical characterization of HL60 cells in cell culture medium (RPMI) and PBS buffer containing 0.5% (w/v) methylcellulose (MC-PBS). (A) Deformation *vs.* cell size scatter plots (red) of RT-DC performed in RPMI using flow rates as indicated. Reservoir data denotes cells under minimal stress. White contour lines circumference 80% of each cell population around distribution maximum. (B) Deformation *vs.* cell size scatter plots (blue) of RT-DC performed in MC-PBS using flow rates as indicated. Red contour lines are identical copies of the white contour lines representing cell deformation in RPMI medium. Insets show representative brightfield images of HL60 cells inside reservoir and channel, respectively. Scale bar is 10 μm. Each data point represents a single cell. Colour shade in scatter plots indicates a linear density scale from min (light red and blue) to max (dark red and blue). Experiments are conducted in PDMS chips with a 300 μm long channel and 20 μm × 20 μm squared cross-section.

0.077 ± 0.017 (Fig. 1B, centre and right panel). In order to illustrate this disparity, we superimposed the deformation *vs.* cell size distribution with the contour lines reflecting 80% of RPMI peak density (red and white solid lines in Fig. 1A and B).

We were interested in the question, if cytoskeletal modifications of HL60 cells can also be detected if mechanical measurements are carried out in cell culture media. So far, most assays require dedicated buffers, *e.g.*, PBS complemented with Pluronic surfactant[14,23] or MC-PBS to reduce cell–surface as well as cell–cell interactions and to adjust solvent density or viscosity to impede cell sedimentation and to ensure a sufficient hydrodynamic stress amplitude.[13] In contrast to cell culture media, these buffers usually lack nutrition and other supplements, which potentially leads to cell starvation and to a misinterpretation of results due to unphysiological conditions.

Here, we exposed HL60 cells to 10 μM CytoD to inhibit actin polymerization (see Materials and methods) and performed RT-DC after resuspension in RPMI and MC-PBS, respectively. In MC-PBS, cells respond with an increase in deformation relative to the DMSO vehicle (Fig. S2) as expected, and also suggested in previous work.[27–29] In RPMI we observe the same trend of increasing deformation in response to CytoD but of lower magnitude (Fig. 2A and Fig. S3). Our findings are confirmed by representative brightfield images that display an increased deformation of cells after CytoD treatment (Fig. 2A, insets).

A statistical analysis of experimental triplicates of a total of 13 476 cells (MC-PBS) and 9901 cells (RPMI) confirms the observed trend. Here, a significant increase in deformation is found between the DMSO vehicle (d = 0.073 ± 0.002, mean ± standard error of the mean, SEM) and the CytoD treatment (d = 0.097 ± 0.003) under MC-PBS conditions (Fig. 2B, left panel, blue data points) but also when performing the measurements in RPMI. Here, our data yields d = 0.025 ± 0.001 for the CytoD sample and d = 0.0160 ± 0.0002 for the DMSO vehicle (Fig. 2B, left panel, red data points). As expected, no significant differences between the negative control and vehicle are apparent.

In MC-PBS our analysis also reveals a statistically significant reduction in cell size comparing CytoD and negative control (Fig. 2B, centre panel). For RPMI we observe the same but non-significant trend and attribute our results to the membrane permeability of DMSO and the lower amount of filamentous actin in response to CytoD, respectively, both leading to a reduction in structural support. Interestingly, our data show that cells suspended in MC-PBS possess a significantly larger cell size for all conditions (Fig. 2B, centre panel and Fig. S4,

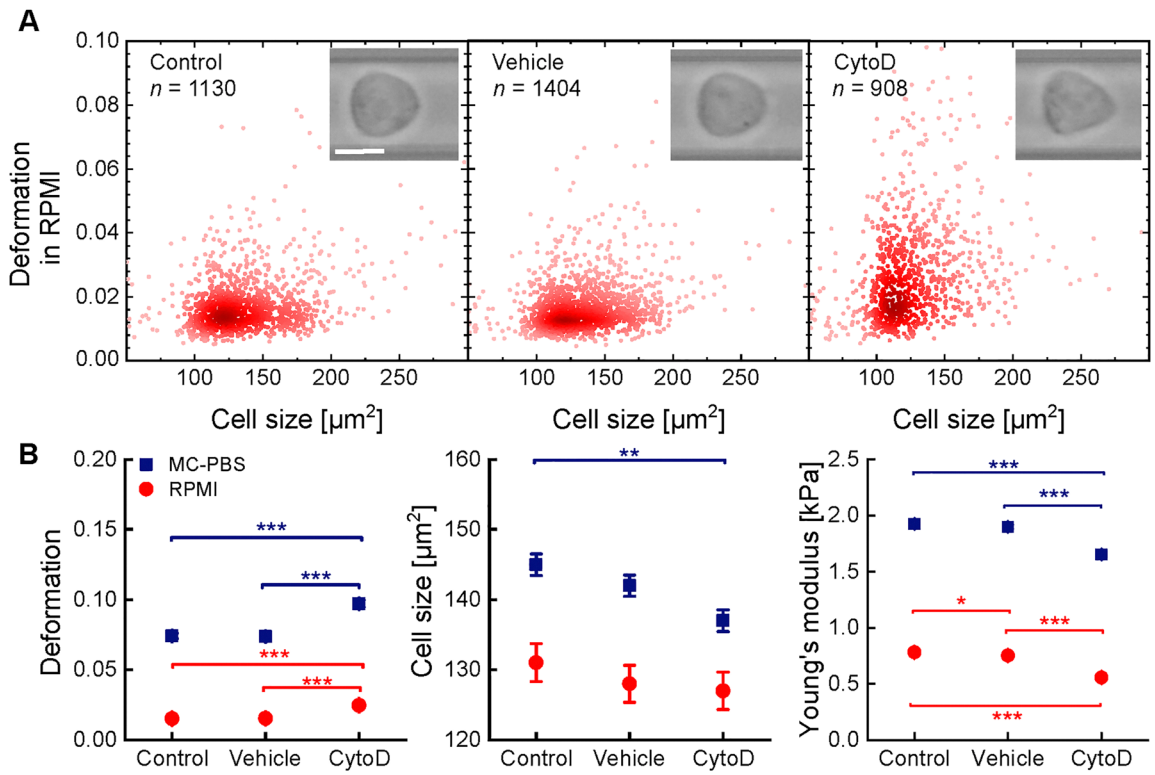

Fig. 2 Mechanical characterization of HL60 cells after cytoskeletal modifications. (A) Scatter plots of HL60 deformation *versus* cell size in RPMI medium as a control (left), in 2.45% (v/v) dimethyl sulfoxide as a vehicle control (centre) and after 10 μM CytoD treatment for 30 min (right). Each data point represents a single cell. Colour shade indicates a linear density scale from min (light red) to max (dark red). Insets show representative brightfield images for each experimental condition. Scale bar is 10 μm. (B) Statistical comparison of three independent experimental replicates in RPMI medium (red) and in MC-PBS solution (blue). Deformation (left), cell size (centre) and corresponding Young's modulus (right) are presented as mean ± standard error of the mean. All Measurements are performed at a flow rate of 80 nL s^{-1}. Event numbers are n = 3460 (control), n = 3623 (DMSO vehicle) and n = 2638 (CytoD) for RPMI data as well as n = 5527 (control), n = 5456 (DMSO vehicle) and n = 2493 (CytoD) for MC-PBS data, respectively. Statistical data analysis is performed using linear mixed models (*p < 0.05; **p < 0.01; ***p < 0.001).

centre panel), which can be explained by the larger deformation resulting from elevated levels in buffer viscosity (see below).

Next, we analysed the effect of CytoD on the elastic modulus of HL60 cells. Analogously to cell size and deformation the HL60 Young's modulus E remains constant upon introduction of DMSO vehicle in MC-PBS (Fig. 2B, right panel, control condition E = 1.92 ± 0.02 kPa and DMSO vehicle E = 1.90 ± 0.02 kPa). However, CytoD (E = 1.65 ± 0.02 kPa) leads to a significantly smaller elasticity in agreement with earlier reports.[28] Cells measured in RPMI exhibit a small but significant decrease in elasticity for the DMSO vehicle compared to the control (control condition E = 0.78 ± 0.01 kPa and DMSO vehicle E = 0.75 ± 0.01 kPa) and a further significant Young's modulus decrease after CytoD treatment (E = 0.56 ± 0.01 kPa).

Surprisingly, for all conditions we find a Young's modulus of HL60 cells, which is significantly higher when measurements are performed in MC-PBS compared to RPMI (Fig. 2B, right panel and Fig. S4, right panel). This is unexpected since cell elasticity as an intrinsic material property should not depend on the medium. To explain this apparent discrepancy, we studied the intracellular F-actin distribution by performing image flow cytometry on several thousand HL60 cells in MC-PBS and RPMI with and without CytoD, respectively. Here, two parameters have been analysed. While texture granularity is a measure for how much of a protein accumulates within a specific part of the cell, the intensity inhomogeneity describes the standard deviation of the intracellular distribution (see Materials and methods).

In RPMI and in presence of DMSO (vehicle) F-actin filaments are distributed homogeneously within the cell cortex (Fig. 3A, inset). This observation is reflected by a narrow distribution in the F-actin inhomogeneity *vs.* texture granularity phase space (Fig. 3A) while projections of both quantities into 1D histograms yield a mean of 49 ± 0.2 and 0.42 ± 0.001, respectively (Fig. 3A, top and right histogram). Having quantified the distribution in each dimension allows us to define thresholds (140 for F-actin inhomogeneity and 0.6 for F-actin texture granularity) and to split the 2D data into four quadrants (Q1 to Q4), which serve as a reference for the remaining conditions. In this reference of HL60 cells suspended in cell culture medium RPMI and treated with the DMSO vehicle, 98.5% of all cells are found in Q4 (Fig. 3A). After CytoD treatment the cell population is characterized by an elevated F-actin texture granularity as well as F-actin inhomogeneity (Fig. 3B)

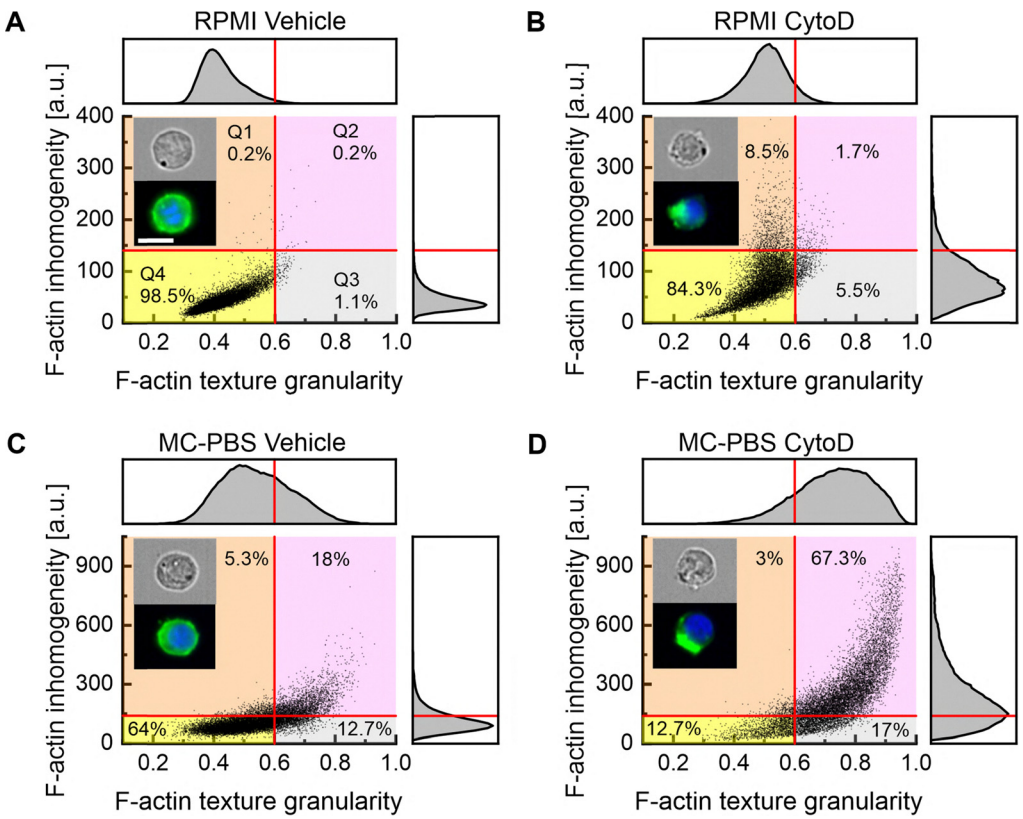

Fig. 3 Intracellular distribution of F-actin. Scatter plot of F-actin inhomogeneity *vs.* F-actin texture granularity for HL60 cells in RPMI for (A) vehicle control (2.45% (v/v) DMSO) and (B) after treatment with 10 μM CytoD for 30 min as well as for HL60 cells in MC-PBS for (C) vehicle control (2.45% (v/v) DMSO) and (D) after treatment with 10 μM CytoD for 30 min. Top histogram of each scatter plot represents a projection of the F-actin texture granularity and the vertical histogram a projection of the F-actin inhomogeneity. Insets show a representative brightfield image (top) and a fluorescence image (bottom) stained with DAPI for nucleus (blue) and Phalloidin for F-actin (green). Scale bar is 10 μm. Each data point represents a single cell. Crosshair (red lines) divides each scatter plot into four quadrants Q1 to Q4 using threshold values 0.6 for F-actin texture granularity and 140 for F-actin inhomogeneity. Thresholds have been identified from the RPMI-vehicle dataset, which serves as a reference.

corresponding to a local aggregation of filamentous actin within the cell cortex (Fig. 3B, inset). The fraction of cells in Q1, Q2 and Q3 increases to 8.5%, 1.7% and 5.5%, respectively.

In MC-PBS and in presence of DMSO (vehicle) the distribution changes substantially compared to RPMI (DMSO vehicle). While cell images reveal only minor alterations in cortical actin (Fig. 3C, inset) the standard deviation in both, F-actin inhomogeneity and texture granularity, increases and the population is shifted from Q4 (64%) into quadrants Q1 to Q3 (5.3% in Q1, 18% in Q2 as well as 12.7% in Q3, Fig. 3C). This suggests that cells have adapted to MC-PBS by slight F-actin remodelling. Interestingly, this adaptation to the external medium can also be observed in RT-DC reservoir data (Fig. 1A and B, left panels) where mean cell deformation is higher in MC-PBS (0.011 ± 0.004) compared to RPMI (0.007 ± 0.003) (mean ± standard deviation) despite the absence of shear stress. Remarkably, after exposure to CytoD 67.3% of the cells are found in Q2 while only 12.7% remain in Q4 (Fig. 3D). Actually, after CytoD treatment F-actin is characterized by a globular accumulation of F-actin as confirmed by fluorescence images independent of the cell-carrier medium (Fig. 3B and D, insets). In fact, CytoD is well known to induce actin bundle aggregation in various cell types.[30–32]

Having described the interplay between inhibition of actin polymerization and its redistribution within the cell in the light of different sample media, we statistically analysed image flow cytometry data from three independent experimental triplicates of a total of n = 91 866 cells (RPMI, Fig. S5) and n = 89 688 cells (MC-PBS, Fig. S6) under these conditions. In general, we observe a statistically significant increase in F-actin inhomogeneity and texture granularity if cells are suspended in MC-PBS (Fig. S7). This result is independent of the treatment and indicates a non-physiological distribution of F-actin inside the cells, rendering the interpretation of mechanical measurements in the absence of nutrition and vitamins challenging. While we observe a significant increase in F-actin inhomogeneity in response to CytoD in RPMI as well as MC-PBS, as expected, the effect size seems to be independent of the suspension buffer used (Fig. 4A). Here, effect size is defined as the ratio of the F-actin inhomogeneities between the CytoD treatment and the vehicle control. For RPMI, we have inhomogeneity values of 78.4 ± 3.0 (CytoD) and 42.2 ± 1.6 (vehicle control) leading to an effect size of approximately 1.9, while we observe for MC-PBS 203.3 ± 7.7 (CytoD) and 109.2 ± 4.0 (vehicle control) resulting in nearly the same effect size.

An analysis of F-actin texture granularity reveals a similar trend in response to CytoD, with a significant increase in amplitude but in contrast also differences in effect size have been observed (Fig. 4B). Here, we report a cell medium effect size of 0.08 (increase in F-actin texture granularity from 0.42 ± 0.01 for RPMI vehicle control to 0.50 ± 0.01 after CytoD treatment), as well as an effect size of 0.19 was observed for MC-PBS samples (increase from 0.53 ± 0.01 for vehicle control to 0.72 ± 0.01 after CytoD treatment).

While the effect size of CytoD on HL60 cells on a molecular scale, *i.e.*, F-actin texture granularity, depends on the suspension medium, the Young's modulus as an intrinsic material property seems to be robust against these external variations (Fig. 2B, right panel). In a subsequent step, we investigated the role of medium viscosity, flow rate and hydrodynamic stress on cell elasticity measured by RT-DC.

Our microfluidic system enables adjusting the flow rate over three orders of magnitude from 0.4 nL s^{-1} to 400 nL s^{-1}. At the smallest possible flow rate deformation is low and comparable for both suspension media resulting to d = 0.009 ± 0.001 for RPMI at 4 nL s^{-1} (Fig. 5A, red data points) and d = 0.012 ± 0.001 for MC-PBS at 0.4 nL s^{-1} (Fig. 5A, blue data points). With increasing flow rate, cells suspended in MC-PBS show a

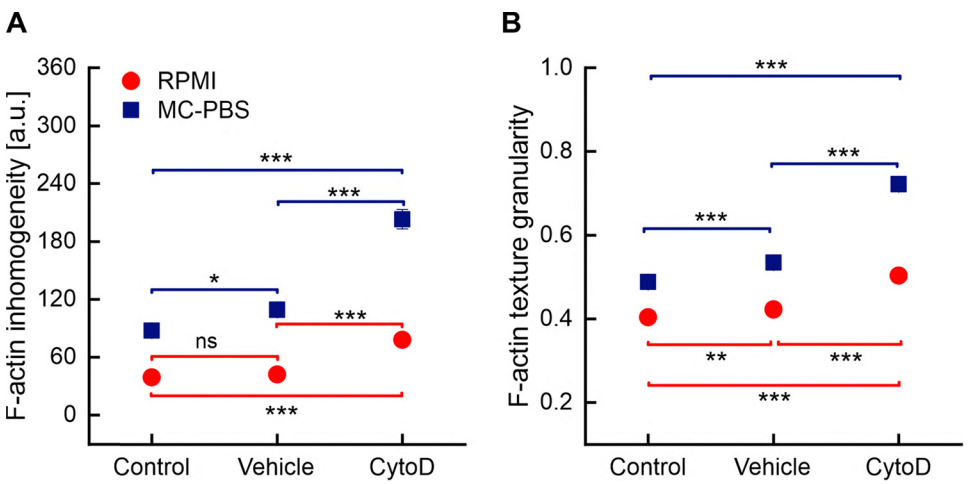

Fig. 4 RPMI and MC-PBS fluorescence-based morphological comparison. Statistical analysis of three independent biological replicates for (A) F-actin inhomogeneity and (B) F-actin texture granularity of HL60 cells suspended in either RPMI (red circles) or MC-PBS (blue squares) at control, DMSO vehicle (2.45% (v/v)) and 10 μM CytoD conditions. Event numbers for RPMI are n = 33 713 (control), n = 32 374 (DMSO vehicle) and n = 25 779 (CytoD) and for MC-PBS n = 27 462 (control), n = 33 890 (DMSO vehicle) and n = 28 316 (CytoD). Statistical data analysis is performed using linear mixed model (*p < 0.05; **p < 0.01; ***p < 0.001).

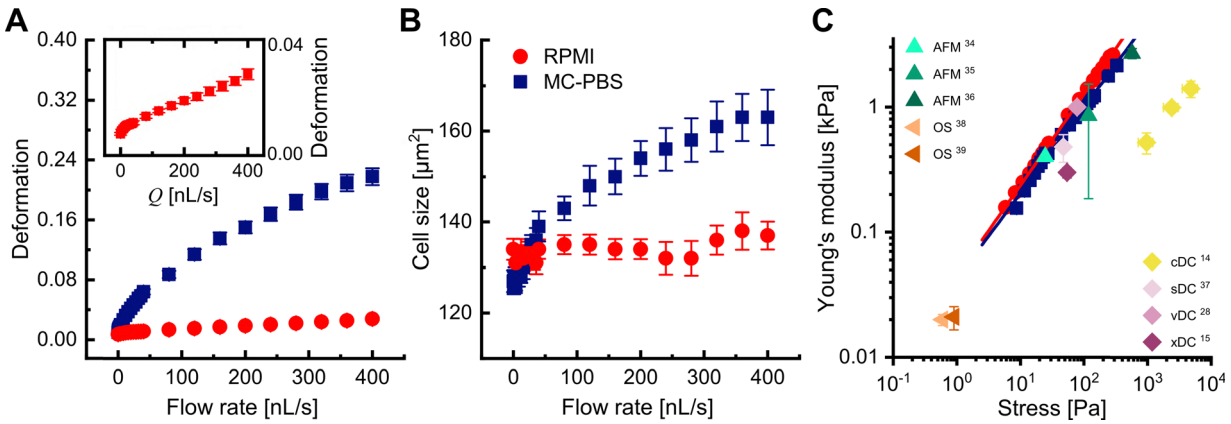

Fig. 5 Stress-stiffening of HL60 cells. Statistical analysis of (A) deformation *vs.* flow rate, (B) cell size *vs.* flow rate and (C) Young's modulus *vs.* external stress of HL60 cells suspended in RPMI medium (red) and MC-PBS buffer (blue) under control conditions. The inset in (A) highlights the small deformation variations relevant for RPMI data. The data originates from 147 experiments at 29 flow rates (MC-PBS) and 20 flow rates (RPMI), respectively, where each data point represents an experimental triplicate consisting of several hundred single-cell mechanical measurements. The solid line indicates a power law fit ($E = E_0 \cdot (\sigma/\sigma_0)^{\alpha}$) to the data in (C). Here, E is the Young's modulus of the cells, σ the hydrodynamic stress, α the stress-stiffening exponent, E_0 the resting Young's modulus (at σ = 1 Pa) and σ_0 = 1 Pa. Error bars represent the standard error of the mean. Additional data points (AFM – atomic force microscopy, OS – optical stretcher, cDC – constriction-based deformability cytometry, sDC – shear flow deformability cytometry, vDC – virtual channel-based deformability cytometry, xDC – extensional flow deformability cytometry, OS – optical stretcher) were taken from literature. For AFM measurements external stress has been derived from the ratio of applied force and contact area, while for deformability cytometry stress is given as the product of strain and Young's modulus (see Methods section). Details for each method are given in Table 2.

considerable higher deformation compared to cells in RPMI. In fact, within the investigated flow rate range the deformation of MC-PBS suspended cells increases by a factor of 18 ($d = 0.218 \pm 0.011$ at highest flow rate of 400 nL s^{-1}) while the corresponding effect in RPMI is merely a factor of 3 ($d = 0.028 \pm 0.002$ at 400 nL s^{-1}). Next, we investigated the effect of suspension medium and flow rate on cell size. Surprisingly, we find a nearly constant cell size of 134 ± 3 μm^2 (mean ± SEM) for RPMI that is independent of flow rate (Fig. 5B, red data points). Using MC-PBS cell size increased from 126 ± 2 μm^2 at 0.4 nL s^{-1} to 163 ± 6 μm^2 at 400 nL s^{-1} (Fig. 5B, blue data points) corresponding to a growth by 29%.

These findings suggest that the higher deformation of MC-PBS suspended cells is attributed to the difference in viscosity between MC-PBS and RPMI. As an alternative explanation, the physiological adaptation of HL60 cells to different media may result in a pronounced softening of MC-PBS suspended cells. In order to distinguish between both explanations, we determined the shear stress σ and HL60 cell Young's modulus. Shear stress σ and shear rate $\dot{\gamma}_{\text{cell}}$ that cells experience while passing the microfluidic channel are derived from finite element method simulations (see Materials and methods) utilizing the full rheological information of MC-PBS and RPMI (Fig. S1). For instance, for RPMI the investigated flow rate range (from 8 nL s^{-1} to 400 nL s^{-1}) translates into mean shear rates 2000 s^{-1} ≤ $\dot{\gamma}_{\text{cell}}$ ≤ 250 000 s^{-1} and mean shear stress values σ from 6 Pa to 285 Pa (Fig. 5C).

At σ = 6 Pa, we observed for cells suspended in RPMI (Fig. 5C, red circles) a Young's modulus of $E = 157 \pm 5$ Pa, which increases steadily with the applied hydrodynamic stress to $E = 2599 \pm 88$ Pa at σ = 285 Pa. In comparison, cells suspended in MC-PBS reveal a Young's modulus that is slightly lower with a difference of 35% to 40% across the entire hydrodynamic stress range (Fig. 5C, blue squares). It seems that the Young's modulus of HL60 cells covers more than one order of magnitude and is subjected to stress-stiffening independent of the measurement buffer used. For both conditions our findings are best described by a power law

$$E = E_0 \cdot \left(\frac{\sigma}{\sigma_0}\right)^{\alpha} \quad (1)$$

Here, α is a stress-stiffening exponent,[33] the prefactor E_0 can be interpreted as cells' resting Young's modulus (strictly speaking at a hypothetical stress of 1 Pa) and σ_0 = 1 Pa. This resting Young's modulus is nearly indistinguishable when cells are measured under RPMI ($E_0 = 44.2 \pm 0.6$ Pa) or MC-PBS ($E_0 = 42.0 \pm 2.3$ Pa) conditions and therefore independent of the external buffer (Table 1).

Next, we investigated the effect of cytoskeletal modifications mediated by 10 μM CytoD on E_0 and α for HL60 cells. DMSO (2.45% (v/v)) was used as a vehicle control and led to a slight reduction in the resting Young's modulus E_0 that is further decreased after CytoD treatment (Table 1). The stress-stiffening exponent α reveals a similar pattern but of opposite sign. In

Table 1 Power law rheology fit parameter. Data is presented as mean ± standard error of the mean. Fit parameter according to eqn (1)

Buffer	Treatment	Intercept E_0 [Pa]	Fluidity α
RPMI	Control	44.2 ± 0.6	0.729 ± 0.004
RPMI	Vehicle	38.7 ± 4.0	0.731 ± 0.026
RPMI	CytoD	14.9 ± 0.9	0.894 ± 0.015
MC-PBS	Control	42.0 ± 2.3	0.687 ± 0.014
MC-PBS	Vehicle	47.3 ± 1.4	0.673 ± 0.006
MC-PBS	CytoD	25.4 ± 0.3	0.761 ± 0.002

presence of MC-PBS, HL60 cells yield $\alpha_{MC\text{-}PBS} = 0.687 \pm 0.014$, which is slightly smaller compared to cells immersed in a RPMI suspension medium ($\alpha_{RPMI} = 0.729 \pm 0.004$). This result could originate from a non-physiological adaptation in the presence of PBS and methylcellulose. Indeed, MC-PBS significantly increases F-actin inhomogeneity and F-actin texture granularity compared to RPMI conditions (Fig. S5–S7) reflecting a cytoskeletal reorganisation. Under exposure of DMSO and CytoD, respectively, both exponents, *i.e.*, α_{RPMI} and $\alpha_{MC\text{-}PBS}$, increase (Table 1) indicating that cells are more susceptible to a hydrodynamic stress when exposed to an external chemical stress. This finding is also confirmed on the molecular scale when analysing F-actin inhomogeneity and F-actin texture granularity (Fig. S7). Interestingly, when the Young's modulus is measured at different hydrodynamic stresses only HL60 cells suspended in RPMI show a substantial reduction in stiffness when exposed to 10 μM CytoD while cells in MC-PBS could not be distinguished from control conditions or the 2.45% (v/v) DMSO vehicle (Fig. S8).

As an alternative to eqn (1) we also investigated if the Young's modulus *vs.* hydrodynamic stress dependency can be described by a linear regression. However, a linear fit proved to be substantially inferior compared to a power law fit in two regards: (i) the 95% prediction interval (*i.e.* the corridor surrounding the fitted line within which 95% of the measured data points can be expected) is smaller for a power law fit compared to linear regression (*e.g.* 100 Pa *vs.* 285 Pa for RPMI data depicted in Fig. 5C). Thus, our Young's modulus data follow the power law model more faithfully. (ii) In a lin–lin representation the curved trajectory of the measured data points becomes apparent (*cf.* Fig. S9A and B) which by definition cannot be fully captured by a linear regression. As a consequence, the residuals of a linear fit show systematic under- and over-prediction rather than the randomness that characterizes a good fit (Fig. S9C and D).

In fact, HL60 cells Youngs's modulus depends on the applied stress level both in RPMI and in MC-PBS, respectively. Probing cells within a stress range of nearly two orders of magnitude demonstrates that generally cells in RPMI indicate a higher stiffness than in MC-PBS at the same stress level. Moreover, irrespective of the used buffer cells' Young's moduli span over at least one order of magnitude depending on the applied shear stress (Fig. 5C). This finding raises the question if the power law stress dependence given by eqn (1) is a universal property of HL60 cells or specific to RT-DC data acquisition. Therefore, we compared our results to other methods like AFM,[34–36] optical stretcher[38,39] and deformability cytometry[14,15,28,37] using Young's modulus values that are taken from literature. For each technique the corresponding stress is calculated specifically (*cf.* Materials and methods section) and absolute values are given in Table 2. Surprisingly, the available literature values on HL60 cell mechanics are in good accordance with the trend predicted by eqn (1), irrespective of the technique and the applied experimental settings. One exception from this rule was reported by Nyberg *et al.*[14] who observed a Young's modulus that is clearly below the prediction of (Fig. 5C, yellow diamond).

Discussion and conclusion

Cell mechanical properties play an important role for our fundamental understanding of biology, physics, pharmacology and medicine.[40–44] Translational applications, however, are often impeded by a lack of standardization and the possibility to compare results from measurements taken at different locations. The variation observed in, *e.g.*, cellular elasticity is currently not fully understood and might be explained by biological diversity, differences in the technologies used and a mismatch in time scales.[24] In order to disentangle this discrepancy, we characterized hundreds of thousands HL60 cells in RPMI cell culture medium (complemented with 10% FCS and 1% P/S) and PBS, the latter complemented with 0.5% (w/v) methylcellulose (MC-PBS). Measurements were performed using RT-DC for experimental triplicates, where cell size, cell deformation and the Young's modulus were analysed at varying flow rates ranging over nearly three orders of magnitude (0.4 nL s^{-1} to 400 nL s^{-1}).[13] For MC-PBS we observed an increase in cell size with increasing flow rate, as expected, while little effect was found for experiments carried out in RPMI. The latter might be explained

Table 2 Mechanical measurements on HL60 cells using various methods. Overview on the current state-of-the-art characterizing HL60 cells by atomic force microscopy (AFM), constriction-based deformability cytometry (cDC), shear flow deformability cytometry (sDC), virtual channel-based deformability cytometry (vDC), extensional flow deformability cytometry (xDC), and optical stretcher (OS). Measurements have been carried out in various cell media, *e.g.*, RPMI (Roswell Park Memorial Institute Medium), MC-PBS (Phosphate Buffer Saline complemented with Methylcellulose) and DMEM (Dulbecco's modified Eagle medium)

Author	Method	Cell medium	Stress [Pa]	Young's modulus [Pa]
Zhang *et al.* (2004)[34]	AFM	Phenol red-free RPMI 1640	24.5	400
Rosenbluth *et al.* (2006)[35]	AFM	RPMI	118	855 ± 670
Sajeesh *et al.* (2016)[36]	AFM	Air	573	2675 ± 241
Nyberg *et al.* (2017)[14]	cDC	0.01% Pluronic F-127 surfactant in RPMI	960 ± 250	520 ± 100
Nyberg *et al.* (2017)[14]	cDC	0.01% Pluronic F-127 surfactant in RPMI	2400 ± 630	990 ± 80
Nyberg *et al.* (2017)[14]	cDC	0.01% Pluronic F-127 surfactant in RPMI	4800 ± 1300	1400 ± 210
Novosedlik *et al.* (2025)[37]	sDC	MC-PBS	47.5	480 ± 120
Panhwar *et al.* (2020)[28]	vDC	MC-PBS + PEG	78.0	1000 ± 60
Armistead *et al.* (2019)[15]	xDC	MC-PBS	54.2	301 ± 29
Ekpenyong *et al.* (2012)[38]	OS	RPMI	0.60	20.0 ± 2.0
Chan *et al.* (2015)[39]	OS	RPMI	0.90	21.0 ± 4.4

by the relatively small deformation amplitudes that hardly impacted on the projected cell size. For cell deformation our data reveal a general increase in amplitude at elevated flow rates with a six-times stronger effect in MC-PBS that can be explained by the higher viscosity of the medium due to the presence of methylcellulose.

Next, we utilized comprehensive understanding of the fluid dynamics inside our microfluidic system, which enables us to determine the mechanical stress distribution on the cell membrane.[45,46] Considering the experimentally available flow rates discussed above we can access a hydrodynamic stress range between approximately 8 Pa and 800 Pa. For both measurement buffers, RPMI and MC-PBS we observe stress-stiffening, *i.e.*, an increase in Young's modulus with increasing hydrodynamic stress. Stress-stiffening is a well-known effect for adherent cells[20,33] and reconstituted *in vitro* networks[47–49] analyzed using different techniques like stress controlled rheometry, microplate based rheometry, atomic force microscopy and oscillatory magnetic twistometry. Previously, it has been shown that cell stiffness increases linearly[20,50] with applied mechanical stress given that a threshold in stress is exceeded.[33] More specifically, cells undergo a transition from a stress independent regime (stress-stiffening exponent $\alpha = 0$) to a linear stress response regime ($\alpha = 1$). In case of 3T3 fibroblasts this transition is reported to occur approximately at an amplitude of 100 Pa.[33] In our case, we observe a nonlinear stress-stiffening exponent smaller than 1, which might be attributed to the fact that previous publications focused on cells in adhesion state while this work investigated cells in suspension.

Distinguishing between linear and nonlinear behavior is challenging. Generally, any nonlinear trend might be approximated by a linear model if the underlying dataset is limited to a narrow shear stress interval. Although it is crucial to investigate cell response to mechanical stress over several orders of magnitude, the applicable parameter space of most techniques is optimized for adherent cells and limited by experimental constraints. Thus, the nonlinear character of stress-stiffening can be obscured. As an alternative approach artificial biopolymer networks mimicking elastic behaviour of cells can be reconstituted inside a rheometer sample chamber and exposed to mechanical stress over several orders of magnitude. For instance, artificial networks made of filamin and F-actin were stressed over four orders of magnitude and confirm the presence of two distinct regimes: at lower stress values stiffness remains constant. After reaching a certain stress threshold, stiffness followed a linear dependence (stress-stiffening exponent $\alpha = 1$).[47,49] However, the linear character of the stress-stiffening regime is likely not a universal feature since artificial networks comprised of filament protein vimentin are characterized by a nonlinear stress-stiffening (exponent $\alpha = 1.55$).[48] A remarkable distinction between experiments conducted on living cells and artificial networks is the transition dynamics between both regimes: reconstituted F-actin networks show a sharp kink in the stress-stiffness curve for the transition from constant stiffness to the linear stress-stiffening regime.[47,49] In contrast, for complex and hierarchically structured entities such as living cells this transition is fuzzy, gradual and requires at least an accessible stress range of one order of magnitude in stress to be completed.[33] Therefore, lower stress-stiffening exponents ($\alpha = 0.729$ in RPMI and 0.687 in MC-PBS) found in this work could be associated by a pending transition into a linear stress-stiffening regime.

In a next set of experiments, we perturbed the cytoskeleton by inhibiting the polymerization of F-actin polymerization using cytochalasin D (CytoD). When comparing HL60 cells before and after exposure to CytoD we found a significant decrease in cell size only for measurements carried out in MC-PBS. Deformation was significantly increased in both sample buffers, while the Young's modulus follows an inverse trend as expected. In order to understand cell softening due to CytoD on a structural level, we explored the changes in filamentous actin using image-based flow cytometry. When HL60 cells were exposed to 10 μM CytoD for 30 min and subsequently stained with Phalloidin our data showed a fragmented and uneven distributed cortical actin network compared to control cells.[30,31] This results into an increased F-actin inhomogeneity and F-actin texture granularity. Due to polymerization inhibition, F-actin is aggregated in particular spots within the cytoplasm instead of being homogenously distributed over the whole cortex. Therefore, cells lose their structural integrity and become softer. Surprisingly in RPMI, the F-actin re-localization effect of the cytoskeleton is significantly smaller than in MC-PBS, which suggests that cells characterized in RPMI medium offer a resistance to cytoskeletal instability and might be less affected by environmental stress factors in general.

In order to better understand the effect of CytoD on cellular mechanics, we went back to our power law rheology experiments and performed RT-DC measurements under varying hydrodynamic stress conditions. Under control conditions, *i.e.*, in the absence of CytoD or DMSO as the vehicle control, our results yield a resting Young's modulus of 44.2 ± 0.6 Pa and 42.0 ± 2.3 Pa for RPMI and MC-PBS, respectively. The fact of having found a resting Young's modulus, *i.e.*, at zero hydrodynamic stress, suggests that there are material properties of cells being independent of experimental conditions. Interestingly this statement is not true in the presence of CytoD. Here, the resting Young's modulus is lower when measurements are carried out in RPMI and it would be interesting to see if these findings can be confirmed for other cell types.

Having established an elasticity–stress relationship for RT-DC measurements, we compared our results to further experimental methods where the Young's modulus of HL60 cells has been determined. After calculating the mechanical stress levels on the cellular membrane, we find that results taken from AFM, OS, sDC, vDC and xDC measurements compare well with our data independent if these experiments have been carried out for cells adhered to a surface or in suspension. In fact, it seems that the underlying power law can be extended to a stress range between approximately 1 Pa[38,39] (optical stretcher) and 600 Pa[36] (atomic force microscope) covering almost three orders of magnitude. The only exception is found in constriction-based deformability cytometry (cDC) measurements reported by Nyberg *et al.*[14] Here,

HL60 cells reveal a significantly lower elasticity. This observation might be understood from a number of methodological differences. First, the constriction size of 5 μm × 10 μm might render cDC measurements more susceptible to the mechanical properties of the cell nucleus. Second, the microfluidic chip has been treated with the surfactant Pluronic F-127 to reduce cell–surface interactions. Third, there is a mismatch in timescales between the cDC data and experiments presented in this study. At a shear stress of approximately 1 kPa reported by Nyberg *et al.* the transition time through the constriction is on the order of 100 ms. In contrast, in RT-DC the passage of a cell takes less than 1 ms (at the highest measured flow rate of 0.12 μL s^{-1} corresponding to a shear stress of approximately 330 Pa).

Taken these arguments together we would like to conclude that the main differences are found in the susceptibility of cDC towards nuclear mechanics since AFM and OS also characterize cells in contact mode or at longer timescales, respectively. With a focus on cytoskeletal mechanics our study therefore suggests that the differences in elasticity values reported in the literature mainly originate from different mechanical stress levels, which could in turn be used to rescale experimental observations onto a unifying master curve.

Materials and methods

Cell culture

Experiments are carried out using the human myeloid precursor cell line HL60 (courtesy of D. E. Olins and A. L. Olins, University of New England). Cells are grown in RPMI 1640 medium (Biowest) along with 10% FCS (Gibco, ThermoFisher Scientific), and 1% penicillin/streptomycin (Biowest). Cells are passaged every 48 hours by harvesting and are resuspended into fresh medium to a final concentration of $\sim 0.2 \times 10^6$ cells mL^{-1}. All measurements are performed approximately 36 hours after passaging (when the cells are in log phase), while a viability of at least 95% is confirmed using trypan blue. Cells are collected by centrifugation at 200 × RCF for 5 min (Allegra X-15R, Beckman Coulter), and around $1{\cdot}10^6$ cells are used for each experimental replicate. Cell cultures are tested to be mycoplasma free regularly.

Compound treatment

Cytochalasin-D (CytoD) is a cell-permeable toxin that inhibits actin polymerization into filaments. A stock of 400 μM was prepared by dissolving 1 mg of CytoD (Sigma-Aldrich) in 99.5% dimethyl sulfoxide (DMSO, Carl-Roth). In our investigations, we employed two distinct measurement buffers: (a) 0.5% (w/v) methylcellulose (Sigma-Aldrich) dissolved in PBS (MC-PBS) and (b) RPMI 1640 medium (Biowest). CytoD was diluted in both measurement buffers to a final concentration of 10 μM using 2.45% (v/v) DMSO. After harvesting (as described above), cells are cultured in an incubator at 37 °C for 30 minutes. As a vehicle control, we used measurement buffers complemented with 2.45% (v/v) DMSO, only, while the negative control had no compounds added.

Imaging flow cytometry

An imaging flow cytometer (Amnis, ImageStream^{X}MK I, Luminex Corporation, Austin, Texas, USA) with image acquisition INSPIRE software (version 4.1.387.0, Luminex) was used to quantify the impact of CytoD on the cytoskeleton of HL60 cells. After treatment, cells are washed with PBS followed by centrifugation at 200 × RCF for 5 min. Standard steps for sample fixation, permeabilization, washing and blocking were performed using reagents available from the immunohistochemistry kit (Thermo Fisher Scientific, Waltham, Massachusetts, USA) following the guidelines provided by the manufacturer.

After blocking, cells are stained for 30 min with NucBlue (1 : 10 dilution, Thermo Fisher Scientific) as a nuclear probe and Phalloidin (Actin red 555, 1 : 10 dilution, Thermo Fisher Scientific) was used for filamentous actin (F-actin). After incubation, cells are washed twice with PBS each followed by a centrifugation step at 1000 × RCF for 5 min. In our assays, Phalloidin was measured in the red channel (Ex/Em: 561/575 nm) at 1.2 mW, and NucBlue in the blue channel (Ex/Em: 405/460 nm) at 40 mW laser power. For each experimental condition (control, DMSO vehicle, and CytoD) three biological replicates were analysed.

After data acquisition, image analysis has been performed using the IDEAS software (version 6.2, Luminex). Here, we focused on two parameters, F-actin inhomogeneity and F-actin texture granularity, which are derived from the red channel (Phalloidin). The F-actin texture granularity is the intensity difference between brightest and darkest pixel normalized by the sum of both intensity values. Hence, texture granularity is a unitless quantity between 0 and 1 that describes how much of F-actin localizes and accumulates inside a specific part of the cell. F-Actin inhomogeneity of each cell is the standard deviation of pixel intensity values normalized by the average pixel intensity. Thereby, F-actin inhomogeneity indicates the overall complexity of each cells F-actin distribution. Cells with a high F-actin inhomogeneity show a higher local intensity, *e.g.*, spots, lower values represent a more homogeneous distribution.

Real-time deformability cytometry

Real-time deformability cytometry (RT-DC) for the mechanical characterization of suspended cells was performed using an AcCellerator (Zellmechanik Dresden, Dresden).[13] Briefly, the setup consists of a microfluidic channel made from polydimethylsiloxane (PDMS), which is illuminated by a microsecond-pulsed LED (L1, Zellmechanik Dresden, Germany) and observed by an inverted microscope (Axio Observer A.1, Zeiss, Jena, Germany) attached to a CMOS camera (MC1362, Mikrotron, Unterschleissheim, Germany). Flow rates for sample and sheath are adjusted using a syringe pump (neMESYS 290N, Cetoni, Korbussen, Germany). Cells with a typical diameter of 13 μm translocating through a 300 μm long microfluidic channel with a 20 μm × 20 μm cross-section experience deformation due to hydrodynamic shear and normal stress. With image acquisition and analysis being done in real-time, thousands of cells per second can be studied on the fly. Here, deformation of each

cell is determined from its cross-sectional area and its perimeter[13]

$$\text{Deformation} = 1 - \text{Circularity} = 1 - \frac{2\sqrt{\pi\,\text{Area}}}{\text{Perimeter}}. \quad (2)$$

Cell cross-sectional area is filtered for a range of 50 μm^2 to 300 μm^2. The area ratio, a ratio of convex hull to raw cell contour area, was limited to an excess of 5% max.[13] Moreover, we applied the analytical model of Mietke *et al.* and the numerical model of Mokbel *et al.*[45,46] to extract the cells' Young's moduli. Briefly, the Young's modulus is obtained by solving the inverse problem, *i.e.*, we assume a homogeneous linear elastic material and calculate deformations for a given elasticity, flow rate, channel geometry and buffer viscosity. The results serve as a lookup table in our experiments.

Measurements are performed in both, RPMI and MC-PBS buffers that are filled in 1 mL syringes (Becton, Dickinson, New Jersey, USA). For RPMI measurements, flow rates (sample + sheath) range from 4 nL s^{-1} to 400 nL s^{-1} and for MC-PBS from 0.4 nL s^{-1} to 400 nL s^{-1}. We always apply a fixed ratio between sample flow rate and sheath flow rate of 1 : 3. To ensure stable hydrodynamic conditions for all measurements, we allow for an equilibration of >30 seconds between two flow rates. In the low flow rate regime (below 2 nL s^{-1}) at least 5 min is taken to adopt for the steady state. Flow rates are tuned alternately from low to high and high to low between experimental replicates to exclude time-dependent effects. All RT-DC measurements were performed at 23 °C (room temperature). Data acquisition, image analysis, and the control of the syringe pump are performed using the ShapeIn2 software (version 2.0.5, Zellmechanik Dresden).

Rheological characterisation of measurement buffer

Shear rate-dependent viscosity of both RPMI and MC-PBS was determined using a rheometer (MCR502, Anton Paar, Ostfildern, Germany) in parallel-plate geometry (PP50/TG) for RPMI (complemented with 10% FCS and 1% P/S), and cylinder geometry (CC28.7) for MC-PBS (PBS complemented with 0.5% (w/v) methylcellulose). The temperature was between 24 °C and 25 °C, and shear rates were measured from $\dot{\gamma}$ = 1 s^{-1} to 40.000 s^{-1}. At low shear rates of up to 300 s^{-1}, the viscosity is constant at 23.7 mPa s or 25.3 mPa s for RPMI and MC-PBS, respectively. For higher shear rates, we find that the viscosity η follows a power law

$$\eta = k \cdot \left(\frac{\dot{\gamma}}{\dot{\gamma}_0}\right)^{m-1}, \quad (3)$$

with k being the consistency coefficient, m the flow behaviour index and $\dot{\gamma}_0$ = 1 s^{-1} for reference. For MC-PBS, we find $m_{\text{MC-PBS}}$ = 0.706 and $k_{\text{MC-PBS}}$ = 135.9 mPa s (Fig. S1). With $m_{\text{MC-PBS}} < 1$, the MC-PBS buffer yields a shear-thinning behaviour as reported earlier.[28]

For $\dot{\gamma} < 10\,383$ s^{-1}, also RPMI follows eqn (3) with m_{RPMI} = 0.801 and k_{RPMI} = 7.38 mPa s, while viscosity reaches a plateau at η_{RPMI} = 1.17 mPa s for higher shear rates.[51]

Shear stress determination

Finite element method simulations were performed in COMSOL Multiphysics 6.2 (Comsol Multiphysics) with its computational fluid dynamics (CFD) module. As previously described, we modelled a microfluidic constriction of 20 μm × 20 μm cross-section and 80 μm length, which is sufficient to derive shear and normal stresses on suspended cells for a fully developed laminar flow.[52] The creeping flow interface was utilised, neglecting inertial forces and turbulence in the present regime of low Reynolds numbers, resulting in a Stokes flow. Fluid properties were taken from the rheological characterisation of RPMI as well as MC-PBS (see paragraph on rheological characterisation of measurement buffer). Densities of MC-PBS and RPMI have been determined to 1005 kg m^{-3}. A cell was estimated as a sphere with a diameter between 12.7 μm and 13.7 μm for MC-PBS as well as between 12.9 μm and 13.3 μm for RPMI, corresponding to the projected cell sizes from our experimental mean values for HL60 cells (see Fig. 5B). The cell was positioned in the centre of the constriction. Based on the symmetry of our geometry, simulations could be restricted to 1/8 of the microfluidic channel cross-section, where we assumed a no-slip boundary condition at all surfaces, including the cell membrane. A fully developed flow was established at the inlet with the experimental volumetric flow rates between 0.8 nL s^{-1} and 120 nL s^{-1} for MC-PBS and between 4 nL s^{-1} and 400 nL s^{-1} for RPMI. At the outlet, a constant pressure constraint was applied while the normal flow direction was enforced.

In order to compare RT-DC data to AFM data for the existing literature, the stress mediated by the AFM nanoindenter is calculated from $\sigma_{\text{AFM}} = F_{\text{peak}}/A_{\text{contact}}$.[53] Here, F_{peak} is the peak force applied to the cells in the instant of highest cantilever deflection and A_{contact} the contact area between cell and indenter in the same instant. $A_{\text{contact}} = \pi r_{\text{contact}}^2$ depends on the contact area radius r_{contact}, which in turn depends on the maximum cell indentation depth δ_{AFM} and the geometry of the indenter. In case of probing the cell with a spherical bead (with bead radius r_{bead}) r_{contact} is given by $r_{\text{contact}} = \sqrt{r_{\text{bead}} \cdot \delta_{\text{AFM}}}$. Likewise, in the case of a pyramidal indenter r_{contact} is given by $r_{\text{contact}} = \delta_{\text{AFM}} \cdot \tan(\alpha)/\sqrt{2}$ with pyramid face angle α.[53]

The comparison with data from deformability cytometry measurements is realized by deriving the cellular stress directly from Hooke's law $\sigma_{\text{DC}} = E \cdot \varepsilon$ using the Young's modulus E and the strain ε values as given in the respective reference.

Statistical data analysis

Linear mixed models (LMMs) were implemented to determine statistical significance from experimental replicates with both fixed and random effects, to distinguish populations as well as to observe effects at individual levels. Fixed effects refer to the measured variables, such as deformation, while the replications are assessed as random effects. A pairwise test using R package 'emmeans' is performed to compare the estimated marginal means for different levels. The analysis was conducted in R-Studio (Version 1.3.1093). ShapeOut software

(version 0.9.1, Zellmechanik Dresden) is used to visualize and export the RT-DC data. Origin (OriginPro 2018b) is employed for data plotting.

Author contributions

PN and OO supervised the project. Sample preparation for Imaging flow cytometry and real-time deformability cytometry was done by YK. Imaging flow cytometry experiments were carried out by DB while MHP performed RT-DC measurements. ES, MHP and PN performed rheological measurements and prepared corresponding samples. BF carried out finite element method simulations for shear rate and hydrodynamic stress. ES analysed rheometer data. Data analysis was done by MHP, PN, BF and SG. MHP, OO and PN wrote the manuscript.

Conflicts of interest

OO is co-founder and shareholder of Zellmechanik Dresden distributing the AcCellerator system for RT-DC measurements. All other authors declare no potential conflict of interest.

Data availability

Data for this article, including RT-DC and Imaging Flow Cytometer datasets are available in the Zenodo repository (**https://doi.org/10.5281/zenodo.15266509**).

Supplementary information is available. See DOI: **https://doi.org/10.1039/d5sm00414d**.

Acknowledgements

This work has been funded by the Bundesministerium für Bildung und Forschung under grant agreements 03Z22CN11 and 03Z22C511. We also gratefully acknowledge financial support from the Deutsche Forschungsgemeinschaft (grant agreements 231396381/GRK-RTG1947 and 374031971 – TRR 240) and the Deutsches Zentrum für Herz-Kreislauf-Forschung (grant agreement 81X3400107). Finally, we kindly thank Lucia Wegbünder for carrying out osmolality measurements.

References

1 J. P. Shelby, J. White, K. Ganesan, P. K. Rathod and D. T. Chiu, A microfluidic model for single-cell capillary obstruction by Plasmodium falciparum-infected erythrocytes, *Proc. Natl. Acad. Sci. U. S. A.*, 2003, **100**(25), 14618–14622, DOI: **10.1073/pnas.2433968100**.

2 M. J. Rosenbluth, W. A. Lam and D. A. Fletcher, Analyzing cell mechanics in hematologic diseases with microfluidic biophysical flow cytometry, *Lab Chip*, 2008, **8**(7), 1062–1070, DOI: **10.1039/b802931h**.

3 S. E. Cross, Y. S. Jin, J. Tondre, R. Wong, J. Y. Rao and J. K. Gimzewski, AFM-based analysis of human metastatic cancer cells, *Nanotechnology*, 2008, **19**(38), 384003, DOI: **10.1088/0957-4484/19/38/384003**.

4 M. Koch, K. E. Wright, O. Otto, M. Herbig, N. D. Salinas and N. H. Tolia, *et al.*, Plasmodium falciparum erythrocyte-binding antigen 175 triggers a biophysical change in the red blood cell that facilitates invasion, *Proc. Natl. Acad. Sci. U. S. A.*, 2017, **114**(16), 4225–4230, DOI: **10.1073/pnas.162084311**.

5 N. Toepfner, C. Herold, O. Otto, P. Rosendahl, A. Jacobi and M. Kräter, *et al.*, Detection of human disease conditions by single-cell morpho-rheological phenotyping of blood, *eLife*, 2018, **7**, e29213, DOI: **10.7554/eLife.29213**.

6 M. Kubánková, B. Hohberger, J. Hoffmanns, J. Fürst, M. Herrmann and J. Guck, *et al.*, Physical phenotype of blood cells is altered in COVID-19, *Biophys. J.*, 2021, **120**(14), 2838–2847, DOI: **10.1016/j.bpj.2021.05.025**.

7 S. M. Recktenwald, M. G. M. Lopes, S. Peter, S. Hof, G. Simionato and K. Peikert, *et al.*, Erysense, a Lab-on-a-Chip-Based Point-of-Care Device to Evaluate Red Blood Cell Flow Properties With Multiple Clinical Applications, *Front. Physiol.*, 2022, **13**, 884690, DOI: **10.3389/fphys.2022.884690**.

8 K. Haase and A. E. Pelling, Investigating cell mechanics with atomic force microscopy, *J. R. Soc., Interface*, 2015, **12**, 20140970, DOI: **10.1098/rsif.2014.0970**.

9 D. A. D. Flormann, C. Anton, M. O. Pohland, Y. Bautz, K. Kaub and E. Terriac, *et al.*, Oscillatory Microrheology, Creep Compliance and Stress Relaxation of Biological Cells Reveal Strong Correlations as Probed by Atomic Force Microscopy, *Front. Phys.*, 2021, **9**, DOI: **10.3389/fphy.2021.711860**.

10 J. Guck, R. Ananthakrishnan, H. Mahmood, T. J. Moon, C. C. Cunningham and J. Käs, The optical stretcher: A novel laser tool to micromanipulate cells, *Biophys. J.*, 2001, **81**(2), 767–784, DOI: **10.1016/S0006-3495(01)75740-2**.

11 Z. L. Zhou, T. H. Hui, B. Tang and A. H. W. Ngan, Accurate measurement of stiffness of leukemia cells and leukocytes using an optical trap by a rate-jump method, *RSC Adv.*, 2014, **4**(17), 8453–8460, DOI: **10.1039/c3ra45835k**.

12 D. R. Gossett, H. T. K. Tse, S. A. Lee, Y. Ying, A. G. Lindgren and O. O. Yang, *et al.*, Hydrodynamic stretching of single cells for large population mechanical phenotyping, *Proc. Natl. Acad. Sci. U. S. A.*, 2012, **109**(20), 7630–7635, DOI: **10.1073/pnas.1200107109**.

13 O. Otto, P. Rosendahl, A. Mietke, S. Golfier, C. Herold and D. Klaue, *et al.*, Real-time deformability cytometry: on-the-fly cell mechanical phenotyping, *Nat. Methods*, 2015, **12**(3), 199–202, DOI: **10.1038/nmeth.3281**.

14 K. D. Nyberg, K. H. Hu, S. H. Kleinman, D. B. Khismatullin, M. J. Butte and A. C. Rowat, Quantitative Deformability Cytometry: Rapid, Calibrated Measurements of Cell Mechanical Properties, *Biophys. J.*, 2017, **113**(7), 1574–1584, DOI: **10.1016/j.bpj.2017.06.073**.

15 F. J. Armistead, J. Gala De Pablo, H. Gadêlha, S. A. Peyman and S. D. Evans, Cells Under Stress: An Inertial-Shear Microfluidic Determination of Cell Behavior, *Biophys. J.*, 2019, **116**(6), 1127–1135, DOI: **10.1016/j.bpj.2019.01.034**.

16 J. R. Lange, C. Metzner, S. Richter, W. Schneider, M. Spermann and T. Kolb, *et al.*, Unbiased High-Precision

Cell Mechanical Measurements with Microconstrictions, *Biophys. J.*, 2017, **112**(7), 1472–1480, DOI: 10.1016/j.bpj.2017.02.018.

17 M. Liang, J. Zhong and Y. Ai, A Systematic Study of Size Correlation and Young's Modulus Sensitivity for Cellular Mechanical Phenotyping by Microfluidic Approaches, *Adv. Healthcare Mater.*, 2022, **11**(19), e2200628, DOI: 10.1002/adhm.202200628.

18 R. Gerum, E. Mirzahossein, M. Eroles, J. Elsterer, A. Mainka and A. Bauer, *et al.*, Viscoelastic properties of suspended cells measured with shear flow deformation cytometry, *eLife*, 2022, **11**, e78823, DOI: 10.7554/eLife.78823.

19 R. M. Hochmuth, Micropipette aspiration of living cells, *J. Biomech.*, 2000, **33**(1), 15–22, DOI: 10.1016/s0021-9290(99)00175-x.

20 P. Kollmannsberger, C. T. Mierke and B. Fabry, Nonlinear viscoelasticity of adherent cells is controlled by cytoskeletal tension, *Soft Matter*, 2011, **7**(7), 3127–3132, DOI: 10.1039/C0SM00833H.

21 Y. Xie, N. Nama, P. Li, Z. Mao, P. H. Huang and C. Zhao, *et al.*, Probing Cell Deformability via Acoustically Actuated Bubbles, *Small*, 2016, **12**(7), 902–910, DOI: 10.1002/smll.201502220.

22 K. M. I. Bashir, S. Lee, D. H. Jung, S. K. Basu, M. G. Cho and A. Wierschem, Narrow-gap Rheometry: A Novel Method for Measuring Cell Mechanics, *Cells*, 2022, **11**(13), DOI: 10.3390/cells11132010.

23 J. R. Lange, J. Steinwachs, T. Kolb, L. A. Lautscham, I. Harder and G. Whyte, *et al.*, Microconstriction Arrays for High-Throughput Quantitative Measurements of Cell Mechanical Properties, *Biophys. J.*, 2015, **109**(1), 26–34, DOI: 10.1016/j.bpj.2015.05.029.

24 M. Urbanska, H. E. Muñoz, J. Shaw Bagnall, O. Otto, S. R. Manalis and D. Di Carlo, *et al.*, A comparison of microfluidic methods for high-throughput cell deformability measurements, *Nat. Methods*, 2020, **17**(6), 587–593, DOI: 10.1038/s41592-020-0818-8.

25 P. H. Wu, D. R. Ben Aroush, A. Asnacios, W. C. Chen, M. E. Dokukin and B. L. Doss, *et al.*, A comparison of methods to assess cell mechanical properties, *Nat. Methods*, 2018, **15**(7), 491–498, DOI: 10.1038/s41592-018-0015-1.

26 H. Kagiwada, C. Nakamura, T. Kihara, H. Kamiishi, K. Kawano and N. Nakamura, *et al.*, The mechanical properties of a cell, as determined by its actin cytoskeleton, are important for nanoneedle insertion into a living cell, *Cytoskeleton*, 2010, **67**(8), 496–503, DOI: 10.1002/cm.20460.

27 S. Golfier, P. Rosendahl, A. Mietke, M. Herbig, J. Guck and O. Otto, High-throughput cell mechanical phenotyping for label-free titration assays of cytoskeletal modifications, *Cytoskeleton*, 2017, **74**(8), 283–296, DOI: 10.1002/cm.21369.

28 M. H. Panhwar, F. Czerwinski, V. A. S. Dabbiru, Y. Komaragiri, B. Fregin and D. Biedenweg, *et al.*, High-throughput cell and spheroid mechanics in virtual fluidic channels, *Nat. Commun.*, 2020, **11**(1), 2190, DOI: 10.1038/s41467-020-15813-9.

29 M. Herbig, A. Mietke, P. Müller and O. Otto, Statistics for real-time deformability cytometry: Clustering, dimensionality reduction, and significance testing, *Biomicrofluidics*, 2018, **12**(4), 042214, DOI: 10.1063/1.5027197.

30 B. R. Stevenson and D. A. Begg, Concentration-dependent effects of cytochalasin D on tight junctions and actin filaments in MDCK epithelial cells, *J. Cell Sci.*, 1994, **107**(3), 367–375, DOI: 10.1242/jcs.107.3.367.

31 M. Kim, K. Song, E. J. Jin and J. Sonn, Staurosporine and cytochalasin d induce chondrogenesis by regulation of actin dynamics in different way, *Exp. Mol. Med.*, 2012, **44**(9), 521–528, DOI: 10.3858/emm.2012.44.9.059.

32 K. Lee and K. Song, Actin dysfunction activates ERK1/2 and delays entry into mitosis in mammalian cells, *Cell Cycle*, 2007, **6**(12), 1487–1495.

33 P. Fernández, P. A. Pullarkat and A. Ott, A master relation defines the nonlinear viscoelasticity of single fibroblasts, *Biophys. J.*, 2006, **90**(10), 3796–3805, DOI: 10.1529/biophysj.105.072215.

34 X. Zhang, A. Chen, D. De Leon, H. Li, E. Noiri and V. T. Moy, *et al.*, Atomic force microscopy measurement of leukocyte-endothelial interaction, *Am. J. Physiol.: Heart Circ. Physiol.*, 2004, **286**(1), 359–367, DOI: 10.1152/ajpheart.00491.2003.

35 M. J. Rosenbluth, W. A. Lam and D. A. Fletcher, Force microscopy of nonadherent cells: A comparison of leukemia cell deformability, *Biophys. J.*, 2006, **90**(8), 2994–3003, DOI: 10.1529/biophysj.105.067496.

36 P. Sajeesh, A. Raj, M. Doble and A. K. Sen, Characterization and sorting of cells based on stiffness contrast in a microfluidic channel, *RSC Adv.*, 2016, **6**(78), DOI: 10.1039/C6RA09099K.

37 S. Novosedlik, F. Reichel, T. van Veldhuisen, Y. Li, H. Wu and H. Janssen, *et al.*, Cytoskeleton-functionalized synthetic cells with life-like mechanical features and regulated membrane dynamicity, *Nat. Chem.*, 2025, **17**(3), 356–364, DOI: 10.1038/s41557-024-01697-5.

38 A. E. Ekpenyong, G. Whyte, K. Chalut, S. Pagliara, F. Lautenschläger and C. Fiddler, *et al.*, Viscoelastic Properties of Differentiating Blood Cells Are Fate- and Function-Dependent, *PLoS One*, 2012, **7**(9), e45237, DOI: 10.1371/journal.pone.0045237.

39 C. J. Chan, A. E. Ekpenyong, S. Golfier, W. Li, K. J. Chalut and O. Otto, *et al.*, Myosin II activity softens cells in suspension, *Biophys. J.*, 2015, **108**(8), 1856–1869, DOI: 10.1016/j.bpj.2015.03.009.

40 D. Di Carlo, A mechanical biomarker of cell state in medicine, *J. Lab. Autom.*, 2012, **17**(1), 32–42, DOI: 10.1177/2211068211431630.

41 K. A. Jansen, D. M. Donato, H. E. Balcioglu, T. Schmidt, E. H. J. Danen and G. H. Koenderink, A guide to mechanobiology: Where biology and physics meet, *Biochim. Biophys. Acta, Mol. Cell Res.*, 2015, **1853**(11), 3043–3052, DOI: 10.1016/j.bbamcr.2015.05.007.

42 P. Egan, R. Sinko, P. R. Leduc and S. Keten, The role of mechanics in biological and bio-inspired systems, *Nat. Commun.*, 2015, **6**, 7418, DOI: 10.1038/ncomms8418.

43 H. H. Lin, H. K. Lin, I. H. Lin, Y. W. Chiou, H. W. Chen and C. Y. Liu, *et al.*, Mechanical phenotype of cancer cells: Cell

softening and loss of stiffness sensing, *Oncotarget*, 2015, **6**(25), 20946–20958, DOI: **10.18632/oncotarget.4173**.

44 Y. Li, W. Tang and M. Guo, The cell as matter: Connecting molecular biology to cellular functions, *Matter*, 2021, **4**(6), 1863–1891, DOI: **10.1016/j.matt.2021.03.013**.

45 A. Mietke, O. Otto, S. Girardo, P. Rosendahl, A. Taubenberger and S. Golfier, *et al.*, Extracting Cell Stiffness from Real-Time Deformability Cytometry: Theory and Experiment, *Biophys. J.*, 2015, **109**(10), 2023–2036, DOI: **10.1016/j.bpj.2015.09.006**.

46 M. Mokbel, D. Mokbel, A. Mietke, N. Träber, S. Girardo and O. Otto, *et al.*, Numerical Simulation of Real-Time Deformability Cytometry to Extract Cell Mechanical Properties, *ACS Biomater. Sci. Eng.*, 2017, **3**(11), 2962–2973, DOI: **10.1021/acsbiomaterials.6b00558**.

47 M. L. Gardel, F. Nakamura, J. H. Hartwig, J. C. Crocker, T. P. Stossel and D. A. Weitz, Prestressed F-actin networks cross-linked by hinged filamins replicate mechanical properties of cells, *Proc. Natl. Acad. Sci. U. S. A.*, 2006, **103**(6), 1762–1767, DOI: **10.1073/pnas.0504777103**.

48 Y. C. Lin, C. P. Broedersz, A. C. Rowat, T. Wedig, H. Herrmann and F. C. MacKintosh, *et al.*, Divalent cations crosslink vimentin intermediate filament tail domains to regulate network mechanics, *J. Mol. Biol.*, 2010, **399**(4), 637–644, DOI: **10.1016/j.jmb.2010.04.054**.

49 G. H. Koenderink, Z. Dogic, F. Nakamura, P. M. Bendix, F. C. MacKintosh and J. H. Hartwig, *et al.*, An active biopolymer network controlled by molecular motors, *Proc. Natl. Acad. Sci. U. S. A.*, 2009, **106**(36), 15192–15197, DOI: **10.1073/pnas.0903974106**.

50 N. Wang, I. M. Toli-Nørrelykke, J. Chen, S. M. Mijailovich, J. P. Butler and J. J. Fredberg, *et al.*, Cell prestress. I. Stiffness and prestress are closely associated in adherent contractile cells, *Am. J. Physiol.: Cell Physiol.*, 2002, **282**(3), 606–616, DOI: **10.1152/ajpcell.00269.2001**.

51 T. Wonerow, M. Uhler, J. Nuppnau, J. P. Kretzer and F. Mantwill, Rheologic behavior of bovine calf serum, *Materials*, 2021, **14**(10), 2538, DOI: **10.3390/ma14102538**.

52 Y. Komaragiri, M. H. Panhwar, B. Fregin, G. Jagirdar, C. Wolke and S. Spiegler, *et al.*, Mechanical characterization of isolated mitochondria under conditions of oxidative stress, *Biomicrofluidics*, 2022, **16**(6), 064101, DOI: **10.1063/5.0111581**.

53 D. C. Lin, E. K. Dimitriadis and F. Horkay, Robust strategies for automated AFM force curve analysis – I. Non-adhesive indentation of soft, inhomogeneous materials, *J. Biomech. Eng.*, 2007, **129**(3), 430–440, DOI: **10.1115/1.2720924**.